Fluid inclusion and stable isotope studies of the Kighal porphyry Cu–Mo prospect, East-Azarbaidjan, NW Iran

Vartan Simmonds, Ali Asghar Calagari & Kurt Kyser

Arabian Journal of Geosciences

ISSN 1866-7511
Volume 8
Number 1

Arab J Geosci (2015) 8:437-453
DOI 10.1007/s12517-013-1130-z

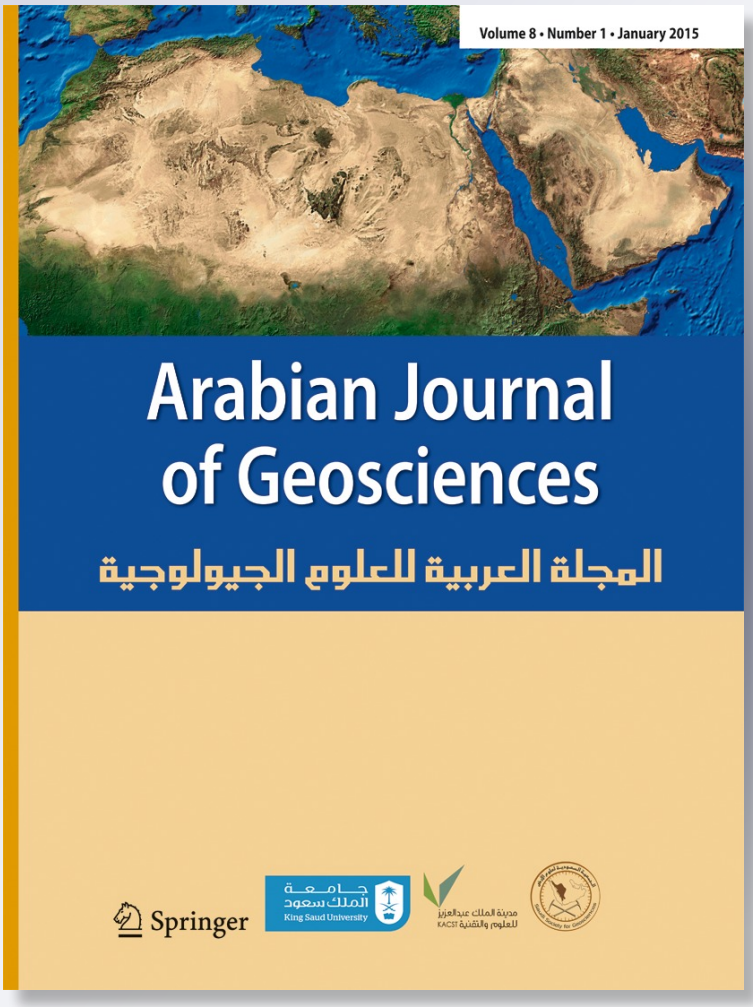

Springer

Arab J Geosci (2015) 8:437–453
DOI 10.1007/s12517-013-1130-z

ORIGINAL PAPER

Fluid inclusion and stable isotope studies of the Kighal porphyry Cu–Mo prospect, East-Azarbaidjan, NW Iran

Vartan Simmonds · Ali Asghar Calagari · Kurt Kyser

Received: 29 April 2013 / Accepted: 16 September 2013 / Published online: 10 October 2013

Abstract The Kighal porphyry Cu–Mo prospect is located to the north of Varzeghan, NW Iran. It is hosted by a quartz monzonite porphyry stock that intruded Eocene volcanic rocks. Hydrothermal activity and associated liquid–vapor immiscibility caused hydro-fracturing and generation of various kinds of quartz–sulfide veinlets. Almost all quartz crystals within these veinlets are fluid inclusion-rich. The entrapped fluids are of four main compositional types: mono-phase vapor-rich, two-phase liquid-rich, two-phase vapor-rich, and multiphase ($L+V+S$). Based on microthermometric studies of fluid inclusions, the salinity ranges from 1.4 to 70 wt% NaCl equivalent, while most of the values cluster between 35 and 70 wt% NaCl equiv. The T_H values of two-phase inclusions homogenizing into liquid and vapor states range between 180–440 and 360–540 °C, respectively. Most of the multiphase inclusions homogenize by halite dissolution with $T_{m(NaCl)}$ varying from 360 to 600 °C, while some of them homogenize by simultaneous disappearance of halite and vapor which show a wider range of T_H (300–600 °C). Inclusions with $T_{m(NaCl)} \gg T_{H(L-V)}$ and higher salinity values may have suffered necking down and/or liquid loss or trapped solid halite crystals. The approximate depth of mineralization and entrapment of the studied inclusions is estimated about >1.0 to 2 km. The principal process responsible for mineralization was liquid–vapor immiscibility and consequent supersaturation of the hydrothermal fluids. Based on stable isotope analyses carried out on quartz–sulfide veinlets, $\delta^{18}O$ (5.4–5.8‰) and δD (−77 to −61‰) values of the ore-bearing fluids, as well as the $\delta^{34}S$ value of a representative pyrite sample (1.3 ‰) are consistent with a predominantly magmatic source.

Keywords Kighal · Fluid inclusion · Homogenization temperature · Salinity · Immiscibility · Stable isotope

V. Simmonds (✉)
Research Institute for Fundamental Sciences, University of Tabriz, Tabriz 51668-76393, Iran
e-mail: simmonds_vartan@yahoo.co.uk

A. A. Calagari
Geology Department, Faculty of Natural Sciences, University of Tabriz, Tabriz 51666-16471, Iran
e-mail: calagari@tabrizu.ac.ir

K. Kyser
Department of Geological Sciences and Geological Engineering, Queen's University, Kingston, Canada
e-mail: kyser@geol.queensu.ca

Introduction

The quartz monzonite porphyry stock at Kighal is located at ~12 km north of Varzeghan, East-Azarbaidjan Province, NW Iran (Fig. 1). Geologically, this area is a part of the Alborz-Azarbaidjan structural zone (Nabavy 1976), Central Iranian domain (Agha Nabaty 2004). This stock lies within the northwestern part of the Cenozoic Sahand-Bazman volcano-plutonic belt of Iran, formed by subduction of Neo-Tethyan oceanic crust beneath the Central Iranian plate during the Alpine orogeny (Berberian and King 1981). This belt hosts most of the major porphyry copper deposits (PCDs) of Iran, including Sar-Cheshmeh (Shahabpour 1982) and Sungun (Calagari 1997, 2004a; Hezarkhani and William-Jones 1998) along with many other smaller deposits and prospects.

The mineral exploration office of the Iranian National Copper Industries Company conducted 15 diamond drillings in the Kighal area and 5 drillings in the adjacent Barmolk area during 2006–2007. During this period, reconnaissance works including geophysical, litho-geochemical, and geochemical investigations on stream-sediments were carried out in the Kighal region. The geology, alteration, mineralization, geochemistry, and genesis of the Kighal Cu–Mo porphyry

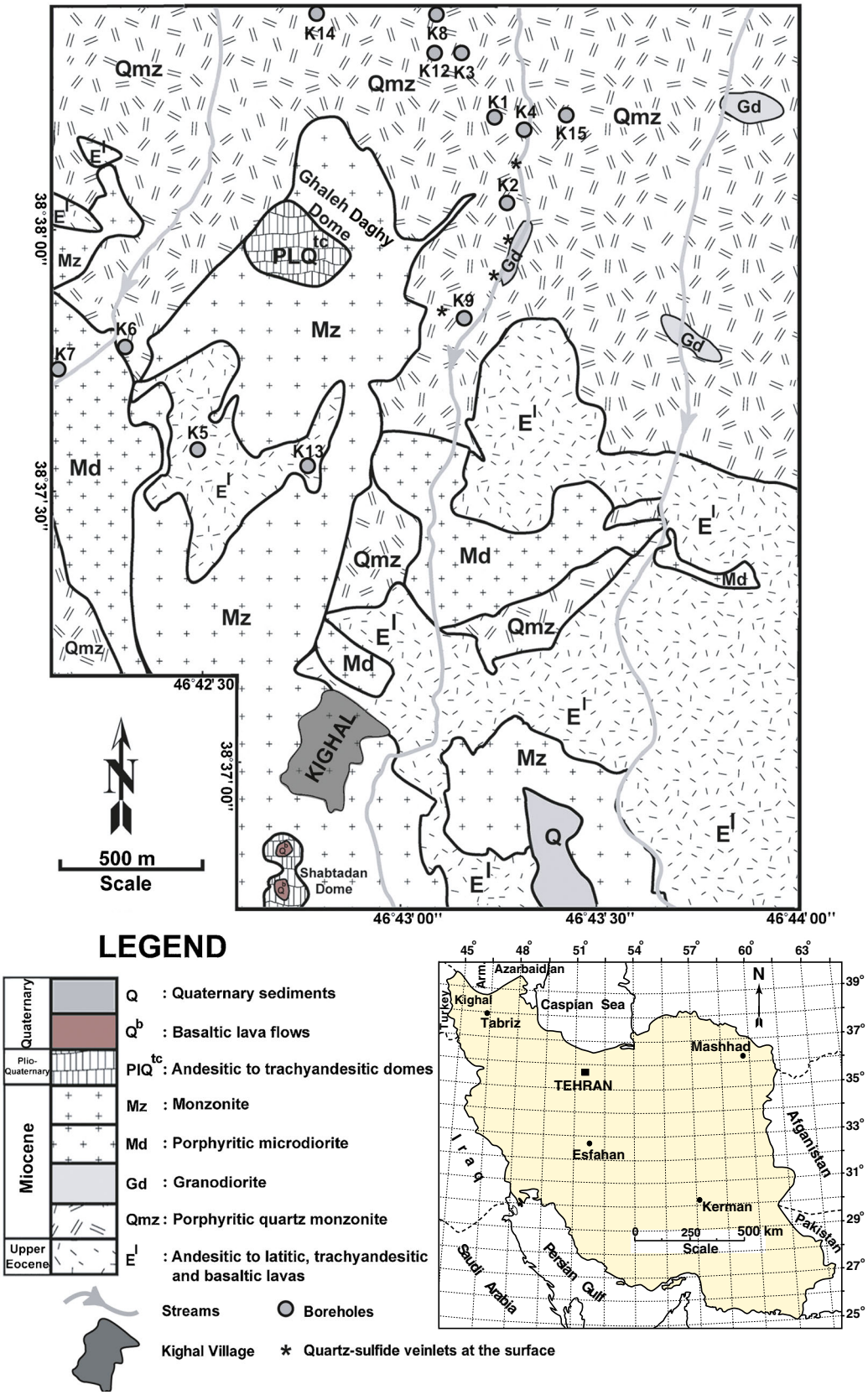

Fig. 1 Modified and simplified geologic map of the Kighal area (after Zarnab Ekteshaf Consultant Engineers 2007), with the locations of boreholes and the main quartz–sulfide veinlets at the surface

prospect were studied by Simmonds (2010, 2013) and Simmonds et al. (2012).

This study aims to elucidate the physical–chemical characteristics (i.e., temperature, pressure, salinity, and stable isotope composition) of the ore-forming fluids through fluid inclusion and stable isotope studies on selected samples from quartz–sulfide veinlets in phyllic and potassic alteration zones (also including some samples from the transitional alteration zone formed by overprinting of phyllic alteration on the potassic alteration zone), as well as sulfate and carbonate veinlets within the Kighal porphyry stock. However, the data used here do not provide the details of changes occurred in fluid properties as a function of time of entrapment within individual host mineral.

Geology

The Kighal porphyry stock which hosts the porphyry Cu–Mo mineralization, intruded andesite–latite and basaltic andesite rocks of upper Eocene (Fig. 1) during magmatic activities of Pyrenean orogenic phase (upper Oligocene–lower Miocene). The resulting hydrothermal activity caused shattering and hydro-fracturing within the cupola of the Kighal stock, leading to the development of various kinds of pervasive alteration zones and Cu–Mo mineralization. The average grades of Cu and Mo in hypogene zone of porphyry stock (based on chemical analyses obtained from Pars Olang Consultant Company) are about 760 and 30 ppm, respectively. However, copper mineralization is more pronounced at the north and northeast of Kighal village (east of Ghaleh-Daghy dome) as manifested by the higher Cu grade in these parts.

This stock along with peripheral host rocks was in turn invaded by three barren sub-volcanic bodies, ranging in composition from granodiorite through micro-diorite to monzonite (Fig. 1). Moreover, six generations of cross-cutting porphyritic dikes with compositions ranging from diorite–quartz diorite to granodiorite, microdiorite, and monzodiorite (in order of intrusion) cut the porphyry stock.

The porphyry stock consists of plagioclase (40–50 %; <5 mm), biotite (0–10 %; <4 mm), and amphibole (0–5 %; <1 mm) phenocrysts in a fine- to medium-grained aplitic quartz-feldspar groundmass, portraying a typical porphyritic texture (Simmonds et al. 2010; Simmonds 2013). This stock and its related cross-cutting dikes display I-type magnesian, calc alkaline to high-K calc alkaline signature and metaluminous to peraluminous geochemical character, being emplaced within an active continental margin setting (Simmonds et al. 2010; Simmonds 2013).

Veinlets and micro-veinlets

The porphyry stock at Kighal underwent multiple intense episodes of shattering and hydro-fracturing manifested by various types of cross-cutting stockwork-like veinlets and micro-veinlets. Based upon mineralogy and paragenetic sequence, they were spatially and temporally classified into five groups, described in Table 1 (Simmonds et al. 2012). Quartz veinlets of v1 and v2 types are surrounded by potassic and phyllic alteration zones and contain the main part of the sulfide (molybdenite, chalcopyrite, and pyrite) mineralization with sulfide contents up to 10 %. Their thickness varies from several millimeters to tens of millimeters. Molybdenite is only present in v1-type veinlets, mainly occurring at their margins. V2 veinlets also display stockwork texture and also contain sphalerite and galena in the peripheral parts of the stock. The dark color of v1-type veinlets is due to presence of fine-grained disseminated sulfides as well as abundant monophase vapor-rich inclusions (Sillitoe 2000; Seedorff et al. 2005). V3-type veinlets are mainly pyritic, with several mm thicknesses and being found in potassic and phyllic alteration zones. V4 veinlets are originally made of anhydrite, containing subordinate amounts of anhedral pyrite crystals. Some of these veinlets are transformed to gypsum through hydration. V5-type carbonate veinlets are mainly found in the peripheral parts of the porphyry stock, surrounded by phyllic alteration zone, and contain pyrite, chalcopyrite, sphalerite, and galena.

Quartz and sulfide crystals within the v1 and v2-type veinlets show intimate association and intergrowth boundaries with each other. Such relationship is also partly evident between carbonate and sulfide crystals in v5-type veinlets. Quartz veinlets of v1 and v2-type are fluid inclusion-rich so they were sampled for microthermometric studies, while v5-type veinlets had no suitable inclusions for this purpose.

Alteration

The stock-related hydrothermal activity led to the development of pervasive zones of potassic, phyllic, argillic, and propylitic alteration zones (Fig. 2; Simmonds et al. 2012) and concurrent Cu–Mo mineralization. The dominant alterations within the porphyry stock are phyllic and potassic, while propylitic alteration zone is predominantly developed within the peripheral volcanic host rocks.

The potassic alteration zone (mainly found in the subsurface diamond-drill cores) is characterized by the occurrence of hydrothermally developed secondary biotite (5–15 %; replacing primary biotite and amphibole) and K–feldspar (0–5 %; occurred as fine-grained anhedral crystals within the groundmass and also marginally replacing plagioclase) along with opaque minerals (magnetite, pyrite, molybdenite, and chalcopyrite).

The phyllic alteration is the most pervasive alteration zone both in superficial outcrops and in subsurface diamond-drill cores. It overlies the potassic zone and covers most of the upper parts of the Kighal porphyry stock. Based on petrographic studies and XRD data, this alteration zone is

Table 1 Different types of veinlets and micro-veinlets present within the Kighal porphyry stock

Type	Veinlets	Paragenesis	Thickness	Occurrence
v1	Dark-grayish quartz veinlets	Quartz, with molybdenite and euhedral and sometimes hydrothermally brecciated pyrite and lesser amounts of chalcopyrite	10–70 mm	Potassic and phyllic alteration zones
v2	Quartz–sulfide veinlets	Quartz, pyrite and chalcopyrite; it also contains sphalerite and galena in the peripheral parts of the stock	2–40 mm	Phyllic alteration zones
v3	Pyrite veinlets and micro-veinlets	Pyrite, almost mono-mineralic	1–10 mm	Potassic and phyllic zones
v4	Anhydrite and gypsum veinlets	Anhydrite or gypsum with lesser amounts of pyrite	5–20 mm	Phyllic alteration zone, especially at the peripheral parts of the stock
v5	Carbonate-sulfide veinlets	Calcite, pyrite, with lesser amounts of chalcopyrite, sphalerite, and galena	2–35 mm	Phyllic alteration zone, especially at the peripheral parts of the stock

characterized by the presence of sericite (20–50 %), pyrite (2–10 %), secondary quartz (20–40 %), and clay minerals (illite). The boundary between potassic and phyllic alteration zones is transitional containing secondary biotite and K–feldspar, sericite, pyrite, and secondary quartz, which implies the superimposition of phyllic alteration on the potassic alteration zone (e.g., Seedorff et al. 2005).

The Argillic alteration zone is developed adjacent to the fracture and fault zones in the upper parts of the porphyry system and suffered high rate of erosion and hence a large part of this zone is wiped out. Based on the XRD data, the main mineral assemblage of this alteration in the area includes kaolinite (<65 %, average 10 %), montmorillonite (<15 %, average 8 %), illite (<61 %, average 14.5 %), and chlorite (<14 %, average 4.9 %). Quartz veinlets in this zone are scarce and thin, only containing insignificant amounts of pyrite and were not suitable for fluid inclusion studies.

Finally, the propylitic zone is characterized by the presence of epidote (1–6 %), chlorite (1–10 %), and calcite (1–8 %) with lesser amounts of sericite, magnetite (<1 %) and locally pyrite (<2 %). There is no quartz veinlet found in this zone.

Moreover, hypogene alteration zones were overprinted by supergene alteration (chiefly argillic) assemblage. Supergene processes developed a leached-oxidized zone above and a sulfide-enriched blanket below the water table.

Mineralization

Sulfide ores principally occurred within potassic and phyllic alteration zones as stockwork-type veinlets and micro-veinlets (quartz–sulfide and sulfide) and as disseminations within the groundmass. Thus, it can be concluded that most of the hypogene sulfide mineralization is controlled by fractures and micro-fractures. The main sulfides are pyrite (1–10 %) and chalcopyrite (0–5 %), accompanied by lesser molybdenite (0–5 %), sphalerite (0–3 %), and galena (0–3 %). Pyrite is the most abundant sulfide mineral and chalcopyrite is the main hypogene Cu–sulfide mineral. Sphalerite and galena are mainly found in the peripheral parts. Stockwork textures and hydrothermal breccias are common both in the surface outcrops and the diamond-drill cores. These may testify to the occurrence of hydro-fracturing caused by the phase immiscibility (boiling) occurred in magmatic-hydrothermal fluids.

During the development of the porphyry system, the chemical weathering and leaching of primary sulfide minerals has led to formation of oxidized and sulfide-enriched supergene zones. The main secondary mineral within the oxidized zone is goethite, which is accompanied by lesser amounts of jarosite and occasionally hematite, as well as malachite and azurite. The sulfide-enriched zone contains low amounts of covellite and bornite, replacing chalcopyrite grains at their margins. In general, the supergene zone has mainly been superimposed on the phyllic alteration zone and there is almost no evidence of its occurrence in the potassic zone.

Microthermometric analysis

Methods and materials

Fluid inclusion studies at Kighal were performed on quartz crystals of v1 and v2-type veinlets collected from different depths of K1, K2, K3, K6, and K7 diamond-drill cores, as well as the outcrops of these veinlets at the bottom of the valley at east of Ghaleh-Daghy dome (Fig. 2). The sampled veinlets were surrounded by phyllic and potassic alteration zones. For implementing this investigation, 20 samples were selected and doubly polished thin sections were prepared. The samples were examined under microscope to determine the distribution pattern, shape, size and phase content, genetic and compositional types of fluid inclusions and the species of daughter minerals. After petrographic examination, the wafers of 10 samples (five samples from v1-type dark-grey veinlets containing molybdenite, pyrite and chalcopyrite in the potassic and phyllic alteration zones, and five samples from v2-type quartz-pyrite-chalcopyrite veinlets in the phyllic alteration zone) were

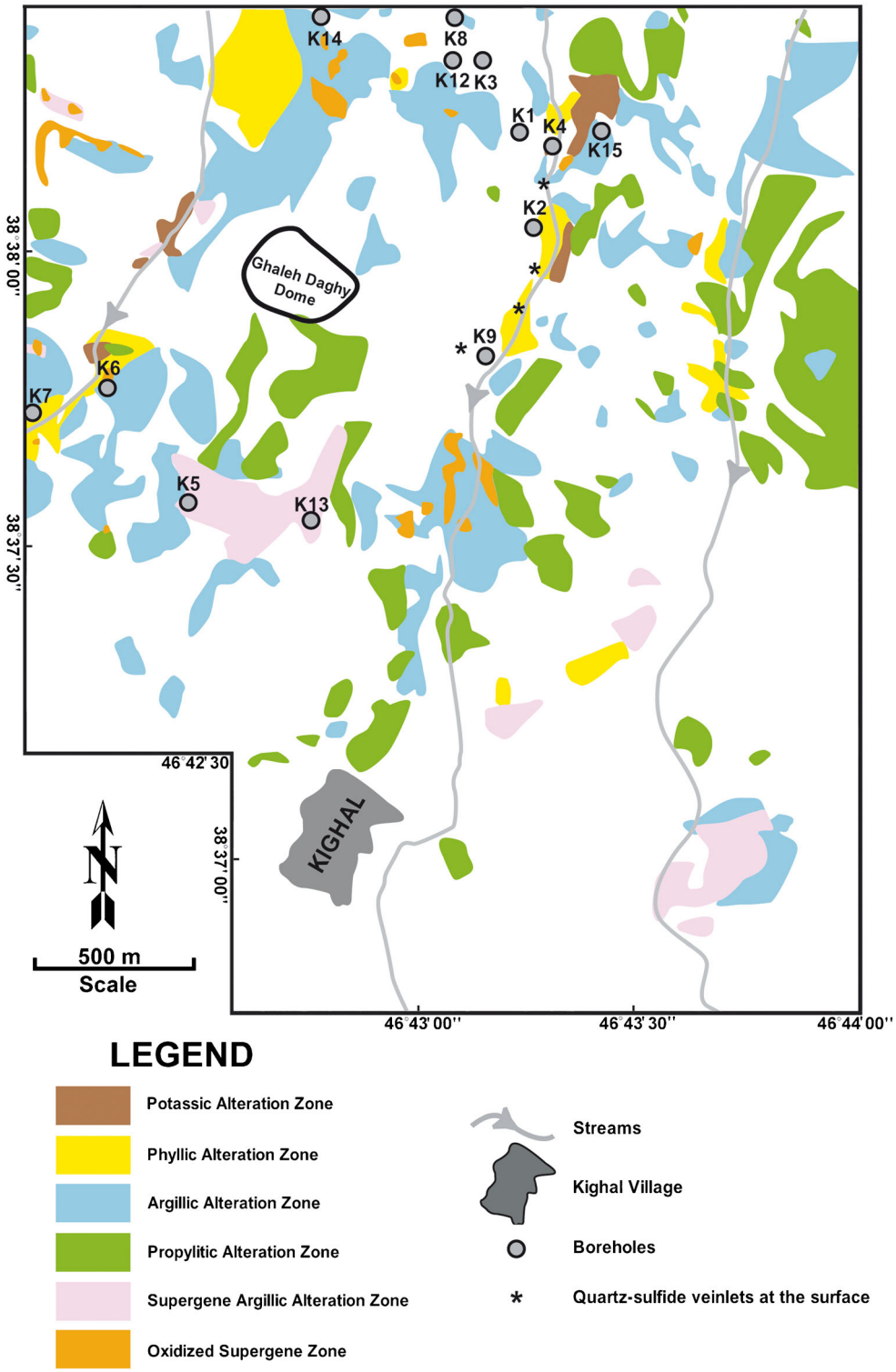

Fig. 2 Modified alteration map of the Kighal area (after Zarnab Ekteshaf Consultant Engineers 2007), with the locations of boreholes and the main quartz–sulfide veinlets at the surface

subjected to microthermometric analysis, using a calibrated and standardized THMS600 Linkam heating-freezing stage, equipped with two heating (TP94) and freezing (LNP) controllers, attached to a Zeiss petrographic microscope and a monitoring video apparatus. The data are reproducible to ±0.2 °C for freezing runs and ±0.6 °C for heating runs.

These analyses were carried out at Mineralographic Laboratory of Advanced Research Center for Ore Materials in Karaj, Iran. Samples were rapidly cooled down to about −100 to −110 °C to detect the possible formation of chlathrate, ice, salt hydrates, and carbonic solid phase. Upon progressive heating, up to five phase transitions were observed in the

inclusions, namely eutectic melting (T_e), melting of the ice ($T_{m(ice)}$), dissolution of the solid phase ($T_{m(solid)}$), mainly halite and sylvite, and total homogenization ($T_{h(total)}$), along with few measurements on melting of a carbonic phase ($T_{m(CO2)}$). The bulk salinity of the fluid was calculated from $T_{m(ice)}$ (Bodnar 1993) or $T_{m(NaCl)}$ (Sterner et al. 1988). The presence of other chemical species (in addition to NaCl and KCl) in the entrapped fluids was estimated based on eutectic temperatures (Borisenko 1977). The density calculations for the studied inclusions were carried out according to Zhang and Frantz (1987).

Results and interpretation

Fluid inclusion petrography

Quartz crystals within almost all types of quartz veinlets at Kighal are fluid inclusion-rich and contain randomly distributed relatively large-sized inclusions (up to 20 μm in size) as well as numerous cross-cutting healed micro-fractures along which a large number of fluid inclusions are aligned (Fig. 3a, b). However, most of the inclusions in the quartz–sulfide veinlets deep in the potassic zone are too small (<5 μm), hosted in the relatively thinner veinlets, and are mainly vapor-rich inclusions, which are not favorable for microthermometric analysis. Anhydrite/gypsum (v4-type) and carbonate (v5-type) veinlets have no recognizable inclusions.

There is no clear evidence of inclusions being trapped along growth zones in quartz crystals, which makes it difficult to identify primary inclusions using criteria of Roedder (1984) and Goldstein (2003). However, randomly scattered and relatively larger inclusions with relatively similar phase ratios (e.g., Hedenquist et al. 1998; Wanhainen et al. 2003; Bodnar 2003; Goldstein 2003; Seedorff and Einaudi 2004; Bouzari and Clark 2006) with no trails of secondary inclusions encircling them were considered as primary, while unambiguously secondary inclusions were all recognizable by their orientation along healed micro-fractures of host crystals. Moreover, some of these secondary inclusions are found along the micro-fractures confined within the host crystals and can be considered as pseudo-secondary inclusions.

In practice, each of the selected similar fluid inclusion assemblages provided narrow ranges of salinity and $T_{H(L–V)}$, indicating their probable simultaneous entrapment. On the other hand, variations in these parameters in all the studied samples revealed that the physical-chemical characteristics of the hydrothermal fluids were changing through time during the development of potassic and phyllic alteration zones.

Based on the terminologies presented by Kranz (1983) and Vollbrecht (1989), secondary and pseudo-secondary fluid inclusions in the studied samples are mainly transgranular, trans-phase and intragranular trails.

Fig. 3 Microphotographs illustrating different types of fluid inclusions within studied samples of v1 and v2-type quartz veinlets (plane polarized light). **a** Numerous trails of secondary inclusions, along with sporadically distributed primary inclusions with relatively bigger size (v2), **b** two intragranular trails of pseudo-secondary inclusions (v1), **c** negative crystal shape mono-phase vapor-rich inclusions (v1), **d** two-phase liquid-rich and mono-phase vapor-rich inclusions with negative crystal shapes (v2), **e** multiphase negative crystal shape inclusions containing daughter minerals (v1), **f** a multiphase inclusion containing halite, sylvite, chalcopyrite (triangular opaque crystal) and an unidentified solid phase (v1), **g** multiphase inclusion containing halite, sylvite, hematite and opaque daughter minerals (v2), **h** multiphase inclusion containing a halite cube and 2 opaque daughter minerals (v2)

The observed inclusions have negative crystal, irregular, elongate, ellipsoidal, rounded, and discoid shapes, in order of abundance (Fig. 3). Necking-down is evident in some inclusions.

Based on their phase content at room temperature, the observed inclusions are mainly categorized into four types, (1) mono-phase vapor-rich, (2) two-phase liquid-rich (aqueous), (3) two-phase vapor-rich, and (4) multiphase and multi-solid, containing a vapor bubble, an aqueous liquid and one or more solids (Fig. 3). There were also some mono-phase liquid inclusions and very few recognizable CO_2-bearing vapor-rich inclusions, where the CO_2 phase was observed as a thin rim around the vapor bubble.

Mono-phase vapor-rich inclusions have bigger size compared to other types (2 to >20 μm) and their distribution is very irregular (Fig. 3c).

The two-phase and multiphase inclusions range in size from 1 to 20 μm (Fig. 3d–h). Most of the two-phase inclusions (containing an aqueous liquid with a vapor bubble) homogenize to liquid phase during heating process.

A large number of fluid inclusions are multiphase ($L+V+S$) ranging in size from 5 to >25 μm (Fig. 3). The most common daughter minerals are halite (identified by its cubic shape, isotropism, and refractive index; Fig. 3e–h) and hematite (red-color blebs; Fig. 3g). Sylvite (smaller cubes with rounded edges; Fig. 3f–g), opaque minerals (Fig. 3e, g, h; in some cases triangular, which might represent chalcopyrite; Fig. 3f) and most likely anhydrite (transparent rod-shape) are other solid phases present within the inclusions. The size of the halite daughter minerals ranges from 1 to 5 μm. In general, up to five solid phases have been observed in a single inclusion and inclusions with two and three daughter minerals are common.

Since there is no hematite within the quartz veinlets, the presence of hematite blebs as daughter crystals within the studied inclusions may be due to post-entrapment diffusion of hydrogen through the inclusion wall after the entrapment of a fluid with high levels of dissolved Fe (most likely in the form of $FeCl_2$) (Roedder 1984; Mavrogenes and Bodnar 1994; Wilkinson 2001). Meanwhile, the presence of chalcopyrite and opaque daughter minerals within the fluid inclusions, as well as the occurrence of these minerals within the studied quartz veinlets confirms that these inclusions contain samples

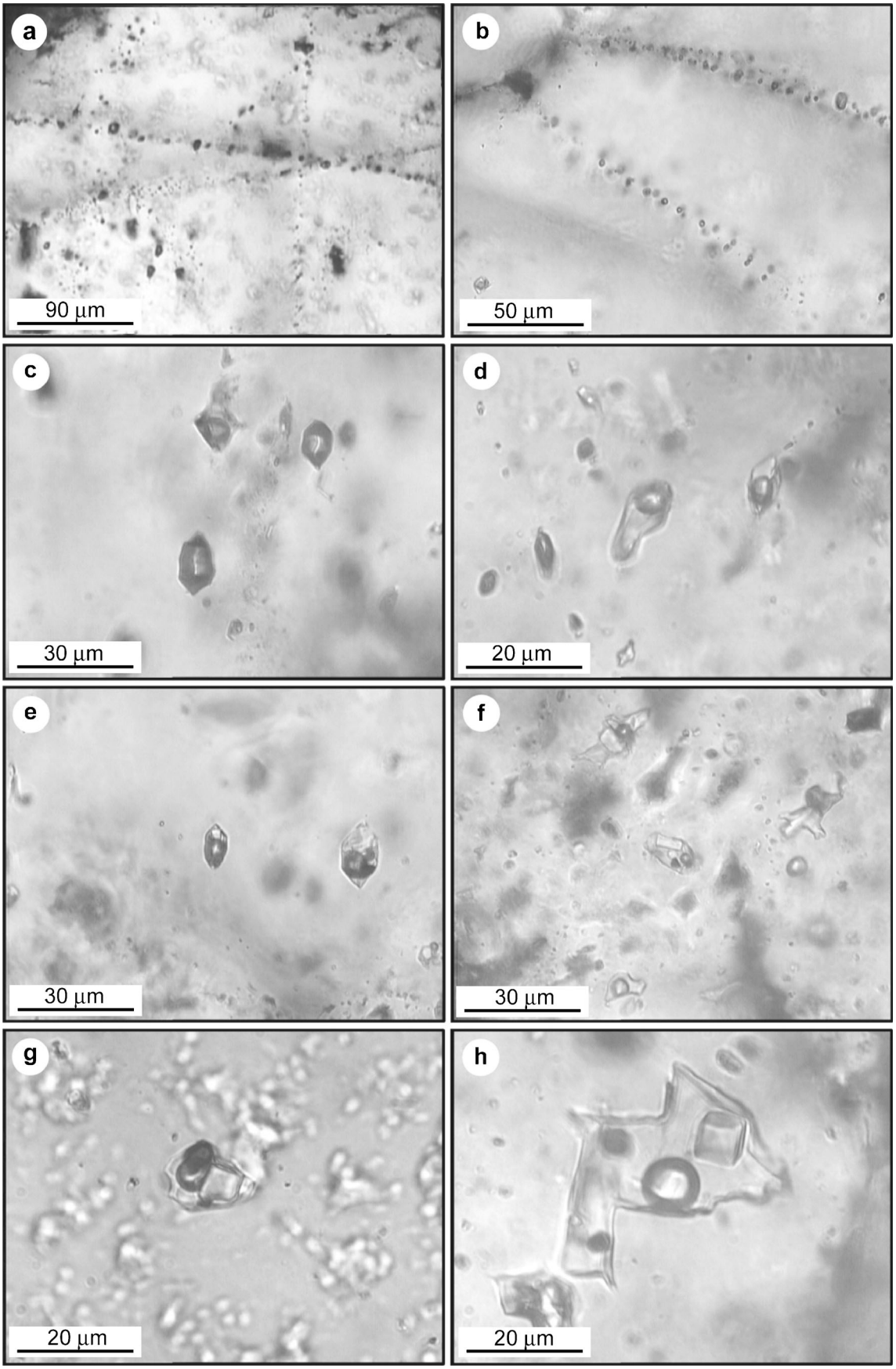

of ore-forming fluids. These opaque daughter minerals may represent trapped solid phases or can be a result of precipitation from trapped fluid during degassing or other changes within the inclusion, as they do not show dissolution during heating process.

The approximately estimated degree of fill (the volumetric proportion of liquid to the total volume of the inclusion) for type 2, 3, and 4 inclusions are about 0.6–0.7, 0.15–0.2, and 0.1–0.3, respectively (Shepherd et al. 1985). Most of the thermometric analyses were carried out on fluid inclusions of type 2 and type 4, which were preferentially primary and had relatively large size (>7 μm up to 20 μm).

Salinity determination

Freezing-based salinity measurements were principally carried out on type 2 (halite-free liquid-rich) inclusions. Salinities of multiphase inclusions were calculated using the melting temperature of halite daughter minerals.

On freezing mode, the measured first melting point values for the majority of the two phase fluid inclusions were mainly within the range of −52 and −45 °C, with some values varying from −35 to −30 °C, which may indicate the presence of a polysaline and multi-cation fluid containing Ca, Mg, and Fe chlorides in addition to NaCl and KCl (Borisenko 1977; Chen et al. 2011). $FeCl_2$ presence is also conceivable from observed hematite blebs within the fluid inclusions. Calcium and magnesium might be supplied during the potassic alteration and destruction of Ca– and Mg–silicates (Ulrich et al. 2001; Rusk et al. 2004) or just the saline fluid was in equilibrium with Ca–Mg silicates. The last melting point of the ice was about −5 to −0.7 °C.

The melting of hydrohalite could only be observed in some of type 2 inclusions, with melting temperature ranging from −21.2 to −19.5 °C. Because of the low proportion of liquid in multiphase solid-bearing inclusions, the disappearance of hydrohalite and the final melting of ice were difficult to observe.

The identified CO_2-bearing inclusions were vapor-rich with a large vapor bubble and a thin rim of CO_2-liquid surrounded by an aqueous phase, which made it quite difficult to detect and measure carbonic phase melting ($T_{m(CO2)}$) and homogenization ($T_{h(CO2)}$) as well as clathrate melting ($T_{m(Clathrate)}$) temperatures. Only for some of these inclusions, it was possible to determine $T_{m(CO2)}$ values, which ranged between −57.2 and −58.4 °C, suggesting the presence of a small fraction of other gases dissolved within the carbonic phase (<5 mol%) (Prokofiev et al. 2010).

The overall salinity estimates range from 1.4 to 70 wt% NaCl equiv (Fig. 4). Most of the values cluster between 35 and 70 wt%, belonging to multiphase inclusions and the values between 23 and 25 wt% are in the second place of frequency, which belong to two-phase liquid-rich inclusions. The lack of halite daughter mineral in the last group is due to the fact that halite saturates at >26 wt% at 25 °C. Also, some of the fluid inclusions show salinities between 1.4 and 7.9 wt% NaCl equiv which are two-phase vapor-rich inclusions.

Homogenization temperature

As previously mentioned, heating experiments were conducted on two groups of fluid inclusions that include two-phase (type 2 and 3) and multiphase (type 4) inclusions. Most of the two-phase inclusions homogenize into liquid state by disappearence of vapor bubble, and the measured $T_{H(L–V)}$ values cluster between 180–340 and 360–440 °C (Fig. 5a). A few percent of two-phase inclusions homogenize to vapor phase. Their $T_{H(L–V)}$ values mainly lie within the ranges of 360–460 °C with the error range of ±20 °C, and few measurements yielding values about 500–540 °C (with the maximum error range less than ±100 °C; Fig. 5b).

Multiphase inclusions also show two types of homogenizations. A large number of them are homogenized by dissolution of halite daughter crystal. They display three distinct clusters of homogenization temperatures, 360–500, 520–600, and 240–280 °C, in order of decreasing abundance (Fig. 5c).

Those multiphase inclusions that homogenized by simultaneous disappearance of halite crystal and vapor bubble or by disappearance of vapor bubble, show sparse homogenization temperatures within narrow ranges of 300–360, 440–460, and 580–600 °C (Fig. 5d).

Taken as a whole, v1-type veinlets yielded higher homogenization temperatures compared to v2 veinlets, which are found in the upper parts of the potassic alteration zone and contain molybdenite mineralization and more mono-phase vapor-rich inclusions, compared to v2 veinlets.

The dissolution temperature of sylvite daughter crystals within multiphase halite–sylvite-bearing inclusions varies between 66 and 110 °C with average value of 89 °C.

None of the opaque daughter minerals underwent dissolution or size decrease during heating process, which can be interpreted as the result of post-entrapment hydrogen diffusion and the change in the redox state of the inclusions (Wilkinson 2001) or may be due to their entrapment from ore-bearing fluid as suspended solid crystals.

In general, such wide ranges of salinities and homogenization temperatures for two-phase and multiphase inclusions are also reported by many workers (e.g., Etminan 1978; Wilkinson 2001; Gonzalez-Partida and Levresse 2003; Calagari 2004b; Landtwing et al. 2010) for typical porphyry copper deposits throughout the world.

Discussion

Interpretation of microthermometric data

Three distinct and separate populations of fluid inclusions are recognizable in salinity versus $T_{H(L–V)}$ plot (Fig. 6): high-

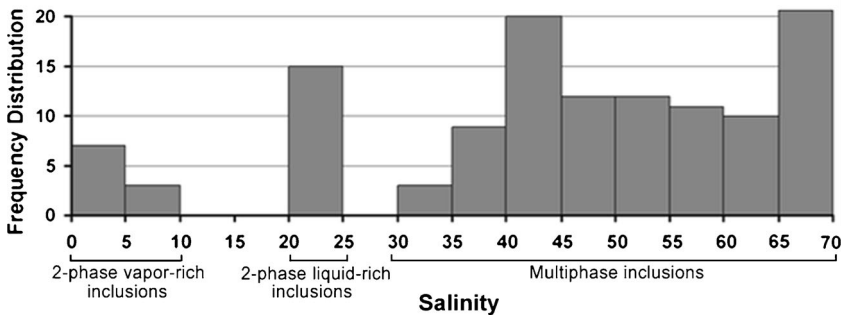

Fig. 4 Frequency distribution of measured salinities of fluid inclusions within quartz veinlets at Kighal

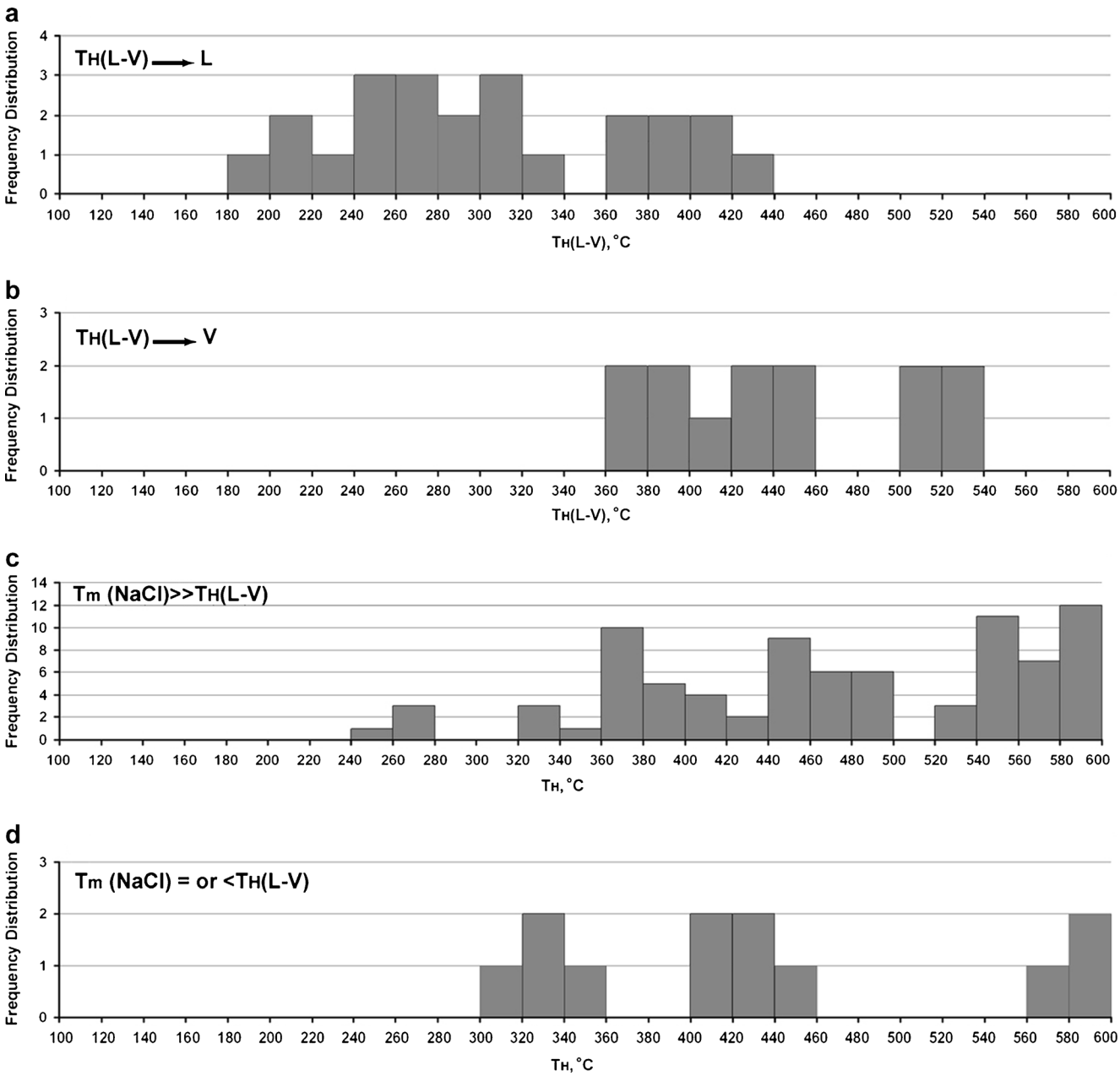

Fig. 5 Frequency distribution histograms for homogenization temperatures measured on fluid inclusions within quartz veinlets of Kighal. **a** two-phase fluid inclusions homogenizing to liquid phase, **b** two-phase fluid inclusions homogenizing to vapor phase, **c** multiphase inclusions homogenizing by dissolution of halite crystal, **d** multiphase inclusions homogenizing by disappearance of vapor bubble

salinity (halite-bearing) with wide range of $T_{H(L–V)}$, moderate-salinity (two-phase) and low-salinity (two-phase) inclusions with relatively narrow ranges of $T_{H(L–V)}$ (compared to high-salinity inclusions). Halite-bearing multiphase inclusions plotted above the NaCl-saturation curve can be resulted in three ways: (1) entrapment from a NaCl-saturated fluid (Roedder 1984), (2) necking down and/or loss of liquid (Audétat and Günther 1999), and (3) entrapping solid halite crystals from hydrothermal fluids. Almost all of these inclusions homogenize by halite dissolution, and just few of them, which lie on or around this curve, show homogenization through vapor or simultaneous vapor-halite disappearance. Inclusions lying under or adjacent to this curve, reflect entrapment from a NaCl-undersaturated or -saturated fluids, respectively.

Based on this diagram, the vapor pressure of NaCl-solutions during the entrapment of low-salinity and moderate-salinity (two-phase) inclusions is estimated below 100 and 250 bars, respectively. Moreover, it can be conceived that hydrothermal fluid experienced saturation (with respect to NaCl) at temperatures about ≤430 °C.

The wide range of $T_{H(L–V)}$ and salinities obtained for the studied inclusions in Figs. 5 and 6 can be explained in several ways. First, it may testify to variations in the physical and chemical characteristics of hydrothermal fluids, or in other words, presence of different fluids at different times, which is rather common in porphyry Cu–Mo deposits. So, quartz crystals have entrapped fluid inclusions with different $T_{H(L–V)}$ and salinity values. Moreover, post-entrapment modifications, such as necking down or leakage can provide inclusions with different phase ratios, salinities and homogenization temperatures. For example, Audetat and Gunther (1999) have demonstrated that many hypersaline fluid inclusions are formed by post-entrapment liquid loss.

Meanwhile, the data points lying above the NaCl-saturation curve in Fig. 6 show distributions along vertical arrays. In other words, in a relatively narrow range of $T_{H(L–V)}$ for such inclusions (especially in the range between 200 and 300 °C), a wide range of salinity is present (35–70 wt.% NaCl). Such a situation can be resulted from entrapment of suspended solid halite crystals from hydrothermal fluids (Bodnar and Beane 1980; Shepherd et al. 1985), and/or isothermal mixing of fluids with different salinities (Shepherd et al. 1985; Wilkinson 2001). For example, Wilkinson (2001) has stated that significant salinity variations are most likely controlled by fluid mixing.

Furthermore, pressurization–depressurization and cooling trends (horizontal arrays) (Wilkinson 2001) are also observable which reveal the pressure fluctuations and alternative dominance of lithostatic and hydrostatic conditions, signifying repeated shattering and hydro-fracturing events.

Further petrographic and microthermometric evidence including the presence of two-phase (liquid-rich and vapor-rich) and halite-bearing multiphase inclusions homogenizing over the same temperature range (Fig. 5), as well as systematic distribution of the densities of liquid- and vapor-rich fluid inclusions (not shown), however, testifies to the occurrence of liquid–vapor immiscibility (boiling) and separation of a high-salinity liquid phase from a low-salinity vapor-rich phase following the initial separation of an aqueous phase from magma at pressures below 1.3 kb (Van den Kerkhof and Hein 2001; Wilkinson 2001) rather than direct segregation of a saline fluid from crystallizing magma (Roedder 1978). If the fluid was directly separated from a crystallizing melt, we could find vapor-rich two-phase inclusions containing opaque daughter minerals, as such phases are less likely found in vapor inclusions produced by immiscibility (Wilkinson 2001). Furthermore, the different phase ratios observed within inclusions of any type can also be attributed to entrapment from a boiling and heterogeneous hydrothermal fluid (Wilkinson 2001), though post-entrapment modifications of the fluid inclusions due to necking down or leakage must not be neglected.

During the occurrence of liquid–vapor immiscibility, fluid salinity gradually increases and the inclusions trap more and more saline fluids. In this condition, entrapment of suspended

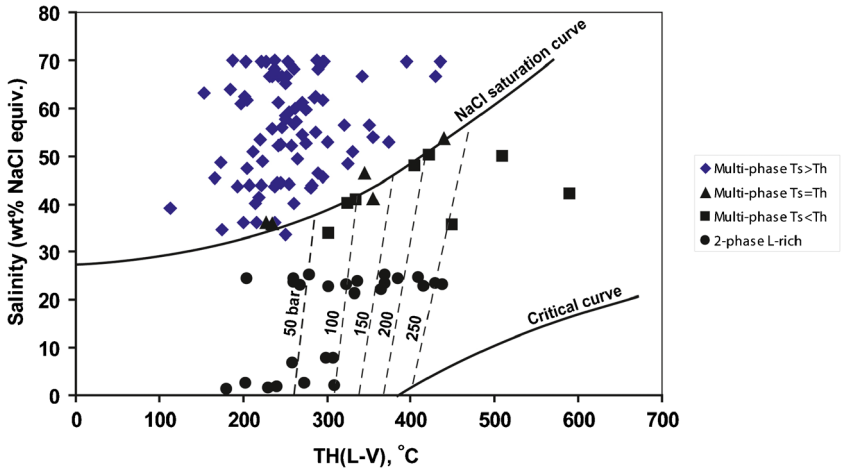

Fig. 6 $T_{H(L–V)}$ vs. equivalent salinities (expressed as wt% NaCl equiv) plot for different fluid inclusion types, illustrating the distribution pattern of the data points relative to the NaCl saturation and critical curves (NaCl saturation and critical curves from Ahmad and Rose 1980, *dashed lines* referring to vapor pressures of NaCl solutions at the indicated temperatures and salinity from Roedder 1984)

halite crystals from the resulted heterogeneous and NaCl-supersaturated hydrothermal fluids is also possible.

Presence of cross-cutting quartz veinlets and micro-veinlets also indicates multiple hydraulic fracturing events during the lifetime of the porphyry stock, most likely related to repeated immiscibility events and various stages of phase separation within the hydrothermal fluids. Consequently, different types and generations of aqueous fluid inclusions with different T_H and salinity values might be entrapped during these events.

In $T_{m(NaCl)}-T_{H(L–V)}$ diagram (Fig. 7), most of the samples are plotted above the diagonal line which similarly can be attributed to entrapment from a NaCl-saturated fluid (e.g., Wilson et al. 1980) at high pressure (Cline and Bodnar 1994; Bodnar 1994), necking down, and loss and leakage of H_2O after fluid entrapment (Sterner et al. 1988; Audétat and Günther 1999) or solid halite entrapment (Bodnar and Beane 1980; Shepherd et al. 1985). Inclusions homogenizing by halite dissolution have entrapped at the low-temperature part of liquid stability field where no coexisting vapor phase is present, whereas inclusions homogenizing by vapor disappearance indicate fluid entrapment at high-temperature part of liquid stability phase in the presence of vapor phase (Roedder and Bodnar 1980; Bodnar 1994; Cline and Bodnar 1994; Zhang et al. 2007).

The discrepancy between $T_{m(NaCl)}$ and $T_{H(L–V)}$ may reflect the relative pressure of the system. For the studied inclusions, this value mainly reaches 100–350 °C. High discrepancies may refer to fluid entrapment at high-pressure condition, which may be present just before the occurrence of hydrofracturing (Cline and Bodnar 1994). On the other hand, necking down (Ahmad and Rose 1980; Audétat and Günther 1999) and/or solid-phase entrapment may also lead to such high discrepancies. Meanwhile, low discrepancies ($T_{m(NaCl)}\sim T_{H(L–V)}$) can be interpreted as an indicator for entrapment of a boiling fluid (Shepherd et al. 1985).

According to Fig. 6, it can be conceived that fluids responsible for the formation of the studied quartz–sulfide veinlets have started boiling at about 440–450 °C, following depressurization of the system. Subsequently a vapor phase has been separated from a saline aqueous liquid phase manifested by inclusions trapped fluids with about 53 wt% salinity. Liquid–vapor immiscibility events recurred episodically until the fluid temperature decreased to ~180–200 °C.

In $T_{H(Final)}$ vs. salinity plot (Fig. 8), halite-bearing multiphase inclusions show positive correlation and a linear trend with constant slope, which is also reported from many other porphyry deposits (Cloke and Kesler 1979; Roedder 1984).

The estimated bulk density for low-salinity two-phase inclusions is about 0.7–0.9 g/cm^3, while it ranges from 0.8 to 1.0 g/cm^3 for moderate-salinity (two phase) inclusions (Zhang and Frantz 1987; Fig. 9). The bulk density of high-salinity halite-bearing inclusions is above 1.0 g/cm^3; halite-bearing inclusions with $T_H=T_{m(NaCl)}$ or $T_H>T_{m(NaCl)}$ have relatively lower and narrow range of density, mainly falling between 1.0 and 1.1 g/cm^3, whereas those with $T_H<T_{m(NaCl)}$ have higher values (1.1–1.3 g/cm^3). It must be noted that there is a negative correlation between density and T_H values of high-salinity as well as moderate-salinity inclusions, indicating that with decreasing homogenization temperature, the density of entrapped fluids increases. Meanwhile, the more the density of inclusions, the higher their salinity is. Such a wide range of estimated bulk density values in coexisting set of inclusions testifies to entrapment from heterogeneous, supersaturated and/or boiling fluids during multiple events of phase immiscibility (Wilkinson 2001).

On this basis, the principal process that ultimately resulted in the deposition of ore minerals in the studied area was liquid–vapor immiscibility and consequent supersaturation of the hydrothermal fluids in a restricted rock volume.

As the occurrence of effervescence and immiscibility is obvious for the studied veinlet samples and hence the aqueous

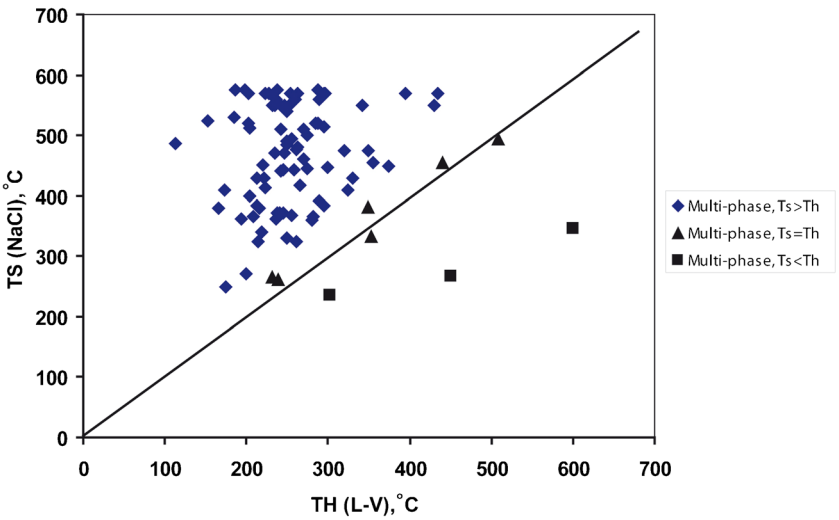

Fig. 7 Liquid–vapor homogenization temperature [$T_{H(L–V)}$] vs. halite dissolution temperature [$T_{m(NaCl)}$] for halite-bearing inclusions at Kighal (the *diagonal line* corresponds to $T_{H(L–V)}/T_{m(NaCl)}=1$; Shepherd et al. 1985)

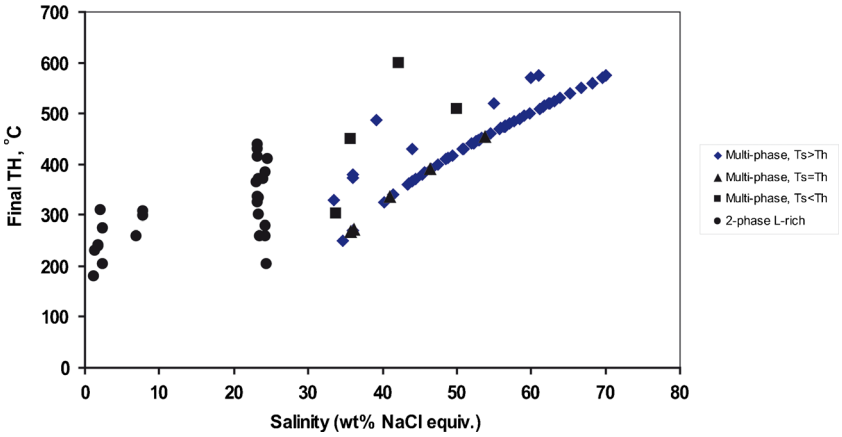

Fig. 8 $T_{H(Final)}$ vs. equivalent salinity (expressed as wt% NaCl equiv) plot, showing the positive linear correlation for halite-bearing multiphase inclusions

inclusions, especially those with $T_{m(NaCl)} \cong T_{H(L-V)}$, have trapped fluids of boiling events; therefore, there is no need to do pressure correction for homogenization temperatures of these inclusions (Roedder and Bodnar 1980; Wilkinson 2001). On the other hand, the presence of coarse-grained quartz crystals along with hydrothermal brecciation evidence within the studied inclusion-hosted veinlets, as well as occurrence of relatively large inclusions (up to 20 μm) signify a near-surface and hence relatively low-pressure environment and thus, the pressure correction for T_H values will be minor (Chen et al. 2011).

The minimum estimated pressures for two-phase inclusions homogenizing around 200–320 °C ranges from 50 to 80 bars corresponding to the hydrostatic depths of 470 to 750 m, respectively. Based on the pressure-T_H diagram for multiphase fluid inclusions (Roedder and Bodnar 1980), the estimated minimum pressure during the entrapment of halite-bearing multiphase inclusions with $T_{H(L-V)}$ equal or almost similar to $T_{m(NaCl)}$ is about 140–200 bars which is equivalent to hydrostatic pressure heads of about 1,300–1,900 m. The wide range of pressure/depth discrepancy between two-phase and multiphase inclusions can be explained by considering the high rate of uplift and erosion in the area during the lifetime of the porphyry mineralization due to its emplacement within the tectonically active Alpine–Himalayan orogenic belt, which has caused the erosion and removal of the main parts of the top of the deposit, so that the potassic alteration zone has outcropped on the surface in some parts. An evidence for this proposition is that four of the studied samples were taken from currently outcropped quartz–sulfide veinlets located in phyllic and potassic alteration zones.

On the other hand, the undeveloped characteristic and low thickness of the sulfide-enriched zone with predominance of covellite and bornite and no trace of chalcocite also implies that the sulfide-enriched blanket is rather young and had not enough time to be developed due to uplift and consequent erosion in the area. So, later low-temperature hydrothermal fluids were trapped at shallower depths (e.g., Rusk et al. 2008) mainly forming low-salinity two-phase inclusions.

However, multiphase inclusions with $T_{m(NaCl)} > T_{H(L-V)}$, show two separate peaks for estimated minimum pressure: one about 100–800 bars and the other about 1,000–2,500 bars. The first group has relatively lower salinities, smaller halite crystals, and lower homogenization temperatures, but the

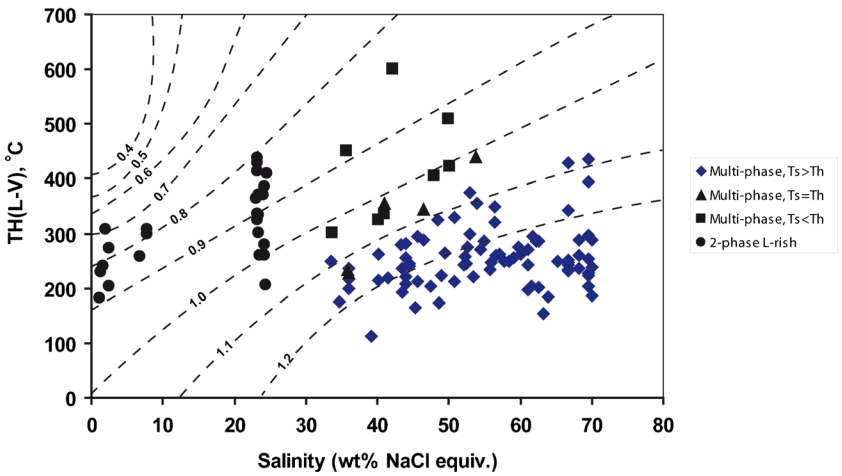

Fig. 9 $T_{H(L-V)}$ vs. equivalent salinities (expressed as wt% NaCl equiv) plot showing densities (in gram per cubic centimeter) of the studied NaCl–H_2O fluid inclusions (Wilkinson 2001). Contours regressed from data generated by the equation-of-state of Zhang and Frantz (1987)

second group is characterized by higher salinities, larger halite crystals and higher $T_{m(NaCl)}$ and $T_{H(L–V)}$. It was shown that these fluid inclusions may have suffered necking down and/or loss of liquid, or have already entrapped solid halite crystals, so it can be concluded that the exceptionally high estimated values up to 2,500 bar especially for the second group of these inclusions cannot be realistic, as two adjacent inclusions in a single quartz crystal cannot entrap two different fluids at such enormously different pressures. Solid halite entrapment from a heterogeneous fluid will lead to shifting of $T_{m(NaCl)}$ to much higher values in a similar $T_{H(L–V)}$. In this case, the variation of salinity values for such inclusions may depend mainly on the size of the trapped solid halite crystal and thus, their salinity and final homogenization temperature will be abnormally higher than other coexisting inclusions and definitely does not represent the real salinity of hydrothermal fluids at the time of entrapment. Necking down and/or loss of liquid can also produce fluid inclusions with large $T_{H(L–V)}$ and $T_{m(NaCl)}$ discrepancies (Ahmad and Rose 1980; Audétat and Günther 1999).

Very few observations of CO_2-bearing inclusions within the studied samples also indicate that phase immiscibility has occurred at shallow depth, as the CO_2 content of magma is higher at much deeper settings and its solubility in felsic magmas declines while the pressure and/or temperature decreases (Lowenstern 2001; Wilkinson 2001). Therefore, the intruding magma will first generate low-salinity CO_2-rich fluid at depth and afterwards, high-salinity low-CO_2 fluid at relatively shallow levels (Shinohara and Kazahaya 1995; Baker 2002; Rusk et al. 2008).

In general, the approximately estimated depth of the mineralization, regardless the false pressures mentioned above, ranges from >1 to 2 km, which is consistent and comparable with the estimated mineralization depths of porphyry deposits in the world (1–5 km; e.g., Pirajno 2009; with the exception of Butte, which has formed at 7–8 km depth in early stages of Cu–Mo mineralization, Seedorff et al. 2005; Rusk et al. 2008) and can be regarded as a shallow porphyry system (Cline and Bodnar 1991).

Stable isotope studies

Methods and materials

Three representative samples of quartz–sulfide veinlets (two from v1-type, one from v2-type veinlets) from potassic and phyllic alteration zones were selected and their quartz grains were handpicked through crushing and leached by HCl acid. Furthermore, three representative separates of pyrite (from v1-type veinlets), gypsum (from v4-type veinlets) and calcite (from v5-type carbonate veinlets) were also analyzed for sulfur and carbon isotopes.

Stable isotope analyses were performed at the Queen's Facility for Isotope Research (QFIR), Queen's University, Canada. Oxygen isotopic composition of quartz grains were measured using a dual inlet Finnigan MAT 252 isotopic ratio mass spectrometer (IRMS). Approximately 5 mg of each sample was used for the analyses. Oxygen was extracted using the BrF_5 method of Clayton and Mayeda (1963).

Hydrogen isotopic compositions of quartz-hosted fluid inclusions were determined based on a modified procedure from Sharp et al. (2001), using TC/EA coupled to a Thermo Finnigan DELTA^{plus}XP mass spectrometer following the extraction of entrapped fluids through thermal decrepitation. Samples weighing 2 mg were loaded in 5×3.5-mm silver capsules and degassed for 1 h at 100 °C, then compacted and loaded into a zero-blank auto sampler. Samples were dropped into a graphite crucible at 1,450 °C, converting the released H_2O into H_2, which was separated by a PORAPLOT-Q gas chromatograph column and measured with a Thermo Finnigan DELTA^{plus}XP IRMS.

Pyrite grains were selected by handpicking from crushed v1-type quartz–sulfide veinlet samples. Sulfur was extracted online with continuous-flow technology, wherein 0.2–0.3 mg of sulfide samples was converted to SO_2 in a Carlo Erba Element Analyzer NCS 2500, with CuO as an oxidant.

Sulfate oxygen was extracted using the technique of Clayton and Mayeda (1963). Sulfur isotopic compositions of sulfide and sulfate samples were corrected using NIST standards 8556 for sulfur and 8557 for sulfur and oxygen.

Calcite from v5-type carbonate-sulfide veinlets were extracted by drilling and analyzed for carbon and oxygen isotopes. Carbonate $\delta^{13}C$ and $\delta^{18}O$ values were measured on CO_2 released from dissolution of 0.5–1.5 mg of sample in 100 % H_3PO_4, using a Thermo Finnigan Gas Bench II attached to a Thermo Finnigan DELTA^{plus}XP IRMS through continuous flow technology. Calcite samples weighing 1–2 mg were loaded in Vacutainer vials, flushed with helium, dosed with 100 % H_3PO_4, and left to react at 72 °C for 4–6 h, after which the CO_2 was analyzed.

Carbon, Sulfur, oxygen, and hydrogen isotopic compositions are reported in standard δ notation in units of per mil relative to the Vienna Peedee Belemnite standard for Carbon, Canyon Diablo Troilite standard for sulfur and Vienna Standard Mean Ocean Water (SMOW) standard for oxygen and hydrogen. The $\delta^{34}S$, $\delta^{18}O$, $\delta^{13}C$, and δD analyses are reproducible to ±0.3, ±0.2, ±0.1, and ±3‰, respectively, as determined by replicate analysis of samples and reference materials. Analytical precision for $\delta^{18}O_{SO4}$ is better than ±0.3‰ (e.g., Chen et al. 2011; Beyer et al. 2012).

Results and interpretation

Oxygen and hydrogen isotopes

Isotopic analyses of oxygen in quartz samples show that $\delta^{18}O$ values vary from 8.1 to 8.9‰ (relative to SMOW) with a

mean value of 8.6‰ (Table 2). Based on these values and the temperature at which quartz veinlets formed (using mean to maximum fluid inclusion homogenization temperatures obtained from microthermometric studies), the calculated $\delta^{18}O$ values of the ore-bearing fluid (using fractionation equation of Matsuhisa et al. (1979) for quartz–H_2O) range from 5.4 to 5.8‰ (relative to SMOW).

The δD values obtained for the fluids extracted from quartz grains which were entrapped within different types and generations of fluid inclusions (including ore-bearing and post-mineralization secondary fluids) range from −77 to −61‰ (relative to SMOW) with a mean value of −67‰, which are significantly higher than the δD values calculated by Calagari (2003) for mid-Tertiary meteoric waters of the region (−110 to −130‰). Although the fluid inclusions analyzed for δD at Kighal, belong to different generations and contain fluids of probably different origins, they nevertheless indicate that the fluids were enriched in ^2H relative to the expected paleo-meteoric values.

The $\delta^{18}O$ values calculated for ore-bearing fluids are consistent with a dominantly magmatic source and lie in the range of $\delta^{18}O$ proposed for primary magmatic waters (Taylor 1979), felsic magmas (Taylor 1992), and andesitic waters (Giggenbach 1992) (Fig. 10).

However, the δD values obtained for the fluids entrapped within the quartz grains is somewhat lower than the δD values reported for felsic magmas (Taylor 1992) and andesitic waters (Giggenbach 1992), though they lie within the primary magmatic box of Taylor (1979; Fig. 10). As the quartz crystals host mixed populations of fluid inclusions with primary and secondary origins trapped at high to low temperatures and different stages, and by taking into account the fact that secondary inclusions may contain post-mineralization fluids with mainly meteoric origin, therefore the extract will contain a mixture of magmatic and meteoric fluids which can lead to deviation from the typical δD values proposed for magmatic waters.

However, geochemical investigation on amphiboles of Yanacocha volcanics in Peru has yielded δD values as low as −60 to −80‰ for magmatic volatiles related to gold mineralization (Chambefort et al. 2013). So, it can be concluded that the ore-bearing fluids during the development of the quartz–sulfides veinlets had predominantly magmatic isotopic signature. The narrow range of $\delta^{18}O$ suggests that isotopic characteristics of the ore-bearing fluids did not significantly change during the formation of these veinlets.

A similar range of $\delta^{18}O$ and δD values are also reported by Hezarkhani and William-Jones (1998) and Calagari (2003) for neighboring Sungun PCD in the region.

Sulfur isotopes

The $\delta^{34}S$ value of the pyrite sample extracted from v1-type quartz–sulfide veinlets is about 1.3‰ (Table 3) which may suggest that the sulfur within ore-forming fluids was derived from a magmatic source (Ohmoto and Rye 1979; Faure 1986).

The $\delta^{34}S_{H2S}$ of the ore-forming fluid is calculated about 0.53–0.63‰, using the $\delta^{34}S$ value of pyrite, fluid inclusion thermometry data and the equation: $\Delta_{(pyrite-H2S)}=0.4(10^6/T^2)$ (Ohmoto and Rye 1979). Accordingly, the $\delta^{34}S_{fluid}$ was estimated about 1.9–2.0‰, using the equation: $\Delta_{(H2S-fluid)}=(1/T)\times10^3$ (Ohmoto and Rye 1979) which also lies within the range of sulfur isotopic composition of fluids derived from granitic magmas (−3 to +7‰; Ohmoto and Rye 1979). So, the sulfur may have derived from parental magma.

The $\delta^{34}S$ value of the gypsum sample derived from gypsum-pyrite veinlets is higher, as expected, being about 15.2‰ (Table 3). The presence of later-stage anhydrite and gypsum (replacing anhydrite through hydration) veinlets indicates that the SO_2/H_2S ratio has subsequently increased due to liquid–vapor immiscibility and removal of reduced sulfur from the fluid phase as sulfide minerals, which may also result in a change in $\delta^{34}S_{fluid}$ (Ohmoto and Rye 1979; Calagari 2003).

$\delta^{34}S$ values of analyzed sulfide and sulfate samples are comparable with those of the majority of PCDs, whose $\delta^{34}S$ values range from −3 to 1‰ and 8 to 15‰, respectively (Ohmoto and Rye 1979).

Carbon isotopes

Calcite veinlets in Kighal porphyry stock mainly occur at the peripheral parts and contain sulfide minerals. The sulfides are

Table 2 $\delta^{18}O$ (of quartz samples) and δD (in inclusion fluids) values from quartz–sulfide veinlets within Kighal porphyry stock. The approximate temperatures of quartz formation were obtained from fluid inclusion data

Sample	Mineral	$\delta^{18}O$ (‰) of quartz (SMOW)	δD (‰) of fluid within inclusions in quartz (SMOW)	Approximate temperature of fluid inclusion entrapment (°C)	Calculated $\delta^{18}O$ (‰) of fluid[a]
A1	Quartz	8.9	−61	425	5.4
B1	Quartz	8.9	−63	450	5.8
B2	Quartz	8.1	−77	490	5.7

[a] $\delta^{18}O_{fluid}$ is calculated using the equation of Matsuhisa et al. (1979) [$\Delta_{(quartz-fluid)}=3.34(10^6/T^2)-3.31$]

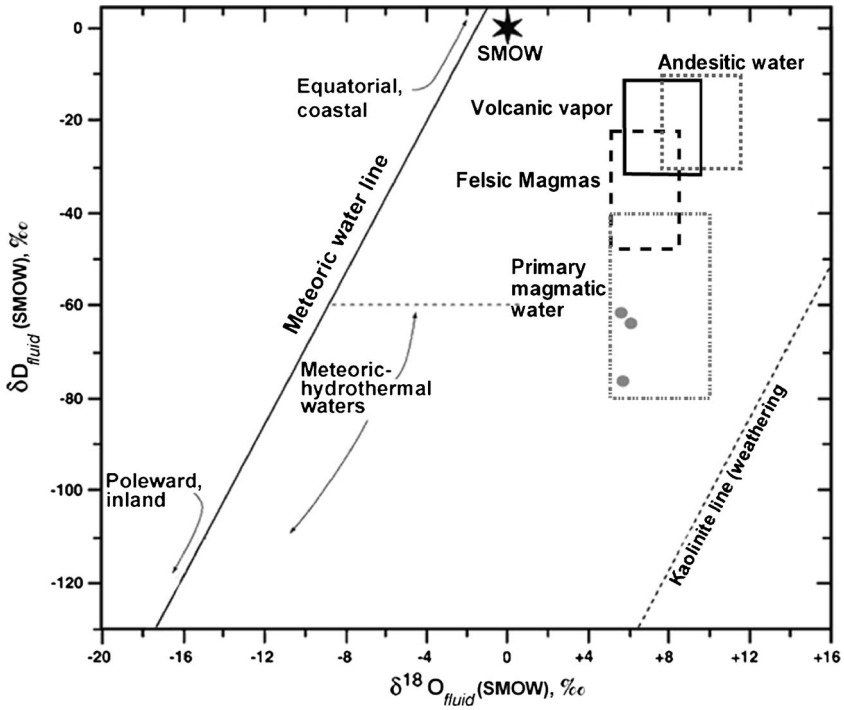

Fig. 10 A plot of δD vs. $\delta^{18}O$ values (*circles*) of the ore-bearing fluids at Kighal. Isotopic compositions of primary magmatic and meteoric waters are from Taylor (1979), felsic magmas from Taylor (1992), andesitic water and volcanic vapor from (Giggenbach 1992) and the meteoric water line is from Craig (1961)

mainly pyrite accompanied by chalcopyrite, sphalerite and galena.

The $\delta^{13}C$ value obtained for the calcite sample is about 1.7‰ PDB, which is close to $\delta^{13}C$ of typically sedimentary carbonates (0±4‰, Ohmoto and Rye 1979). Therefore, the potential source of carbon in the calcite veinlets at Kighal was possibly the dissolution of the upper Cretaceous carbonate rocks, which are cropped out a few kilometers north of Kighal and most likely overlain by Eocene volcanic rocks at the studied area.

Unfortunately, there were no favorable fluid inclusions for microthermometry within these veinlets, so it was not possible to calculate their formation temperature and $\delta^{13}C_{CO2}$. However, since these veinlets contain sulfide minerals, so it can be concluded that the fluid responsible for precipitation of carbonate and sulfide minerals was still high temperature, and therefore, the dominant carbon species within the fluid phase was mainly CO_2, as dissolution reactions of carbonates produce CO_2 at high temperatures and HCO_3^- is produced at surface conditions (Ohmoto and Rye 1979)

The $\delta^{18}O$ value of calcite sample is about 14.3‰ which is isotopically lighter than $\delta^{18}O$ of sedimentary carbonates. The difference may be due to the fact that when CO_2 and carbonate ions derived from the sedimentary carbonate rocks were isotopically equilibrated (through isotopic exchange reaction) with magmatic fluids at high temperatures, their original $\delta^{18}O$ values might have undergone a major shift towards a lower range (Calagari 2003).

Table 3 $\delta^{34}S$ values of a representative gypsum sample (from gypsum–sulfide veinlets) and a representative pyrite sample (from quartz–sulfide veinlets of phyllic alteration zone)

Sample	Mineral	Approximate S wt%	$\delta^{34}S$ (‰) (CDT)
D1	Gypsum	11	15.2
A2	Pyrite	66	1.3

Conclusion

The data obtained from the fluid inclusion studies within quartz samples of quartz–sulfide veinlets in the phyllic and potassic alteration zones at Kighal display remarkable similarity with those obtained from other PCDs across the world, in respect of salinity, homogenization temperature, shape, and phase content. However, the similarities of these aspects at Kighal with those of Sungun PCD (located about 10 km north of the area; Calagari 1997, 2003, 2004b) are much more pronounced. Based upon petrographic and microthermometric evidence, ore-forming magmatic-hydrothermal aqueous fluids had undergone liquid–vapor immiscibility events after severe shattering and hydrofracturing. Moreover, multiple immiscibility episodes can be conceived from the presence of different generations of cross-cutting stockwork-type quartz veinlets within the porphyry stock.

Variations in $T_{H(L-V)}$ and salinity values of the studied fluid inclusions may be attributed to the presence of different fluids at different times through the lifetime of the porphyry mineralization and/or post-entrapment modifications, such as necking down and liquid loss. The approximately estimated depth for

the entrapment of the studied fluid inclusions ranges from >1 to 2 km.

Furthermore, the stable isotope data (O, H, and S) indicate that the ore-forming fluids and their sulfur content are most likely derived from dominantly magmatic source, whereas carbon is probably originated from sedimentary carbonate source rocks.

Acknowledgements The authors would like to express their thanks and appreciations to Prof. John Dilles and the anonymous reviewers for their valuable reviews and helpful recommendations which greatly promoted the manuscript.

References

Agha Nabaty E (2004) Geology of Iran. Geological survey and mineral exploration organization of Iran, Tehran

Ahmad SN, Rose AW (1980) Fluid inclusions in porphyry and skarn ore at Santa Rita, New Mexico. Econ Geol 75:229–250

Audétat A, Günther D (1999) Mobilization and H2O-loss from fluid inclusions in natural quartz crystals. Contrib Mineral Petrol 137:1–14

Baker T (2002) Emplacement depth and carbon dioxide-rich fluid inclusions in intrusion-related gold deposits. Econ Geol 97:1111–1117

Berberian M, King GCP (1981) Towards paleogeography and tectonic evolution of Iran. Can J Earth Sci 18:210–265

Beyer SR, Kyser K, Hiatt EE, Polito PA, Alexande P, Hoksbergen K (2012) Basin evolution and unconformity-related uranium mineralization: the Camie River U prospect, Paleoproterozoic Otish Basin, Quebec. Econ Geol 107:401–425

Bodnar RJ (1993) Revised equation and table for determining the freezing point depression of H_2O–NaCl solutions. Geochim Cosmochim 57:683–684

Bodnar RJ (1994) Synthetic fluid inclusions: XII. The system H_2O-NaCl. Experimental determination of the halite liquidus and isochors for a 40 wt% NaCl solution. Geochim Cosmochim 58:1053–1063

Bodnar RJ (2003) Introduction to fluid inclusions. In: Samson I Anderson A Marshall D (eds) Fluid inclusion-analysis and interpretation, Mineral Assoc Canada, Short Course Series 32:1–9.

Bodnar RJ, Beane RE (1980) Temporal and spatial variations in hydrothermal fluid characteristics during vein filling in preore cover overlying deeply buried porphyry copper-type mineralization at Red Mountain, Arizona. Econ Geol 75:876–893

Borisenko AS (1977) Study of the salt composition of solutions in gas–liquid inclusions in minerals by cryometric method. Sov Geol Geophys 18:11–19

Bouzari F, Clark AH (2006) Prograde evolution and geothermal affinities of a major porphyry copper deposit: the Cerro Colorado hypogene protore, I Región, northern Chile. Econ Geol 101:95–134

Calagari AA (1997) Geochemical, stable isotope, noble gas and fluid inclusion studies of mineralization and alteration at Sungun porphyry copper deposit, East-Azarbaidjan, Iran: implication for genesis. Dissertation, University of Manchester.

Calagari AA (2003) Stable isotope (S, O, H and C) studies of phyllic and potassic-phyllic alteration zones of the porphyry copper deposit at Sungun, East-Azarbaidjan, Iran. J Asian Earth Sci 21:767–780

Calagari AA (2004a) Geology and fracture-related hypogene hydrothermal alteration and mineralization of porphyry copper deposit at Sungun, Iran. J Geol Soc India 64:595–618

Calagari AA (2004b) Fluid inclusion studies in quartz veinlets in the porphyry copper deposit at Sungun, East-Azarbaidjan, Iran. J Asian Earth Sci 23:179–189

Chambefort I, Dilles JH, Longo AA (2013) Amphibole geochemistry of the Yanacocha Volcanics, Peru: evidence for diverse sources of magmatic volatiles related to gold ores. J Petrol 54:1017–1046

Chen H, Kyser TK, Clark AH (2011) Contrasting fluids and reservoirs in the contiguous Marcona and Mina Justa iron oxide–Cu (−Ag–Au) deposits, south-central Peru. Miner Depos 46:677–706

Clayton RN, Mayeda TK (1963) The use of bromine pentafluoride in the extraction of oxygen from oxides and silicates for isotopic analysis. Geochim Cosmochim 27:43–52

Cline JS, Bodnar RJ (1991) Can economic porphyry copper mineralization be generated by a typical calc-alkaline melt? J Geophys Res 96: 8113–8126

Cline JS, Bodnar RJ (1994) Direct evolution of brine from a crystallizing silicic melt at the Questa, New Mexico, molybdenum deposit. Econ Geol 89:1780–1802

Cloke PL, Kesler SE (1979) The halite trend in hydrothermal solutions. Econ Geol 74:1823–1831

Craig H (1961) Isotopic variations in meteoric waters. Science 133:1702–1703

den Kerkhof V, Hein U (2001) Fluid Inclusion petrography. Lithos 55: 27–47

Etminan H (1978) Fluid inclusion studies of the porphyry copper ore bodies at Sar-Cheshmeh, Darreh Zar and Mieduk (Kerman region, southeastern Iran) and porphyry copper discoveries at Miduk, Gozan, and Kighal, Azarbaijan region (northwestern Iran). Int Assoc Genes Ore Depos 5th Symposium, Snowbird, Utah, Proceedings, 88.

Faure G (1986) Principles of isotope geology. Wiley, New York

Giggenbach WF (1992) Isotopic shifts in waters from geothermal and volcanic systems along convergent plate boundaries and their origin. Earth Planet Sci Lett 113:495–510

Goldstein RH (2003) Petrographic analysis of fluid inclusions. In: Samson I, Anderson A Marshall D (eds) Fluid inclusion-analysis and interpretation. Mineral Assoc Canada, Short Course Series 32:9–54.

Gonzalez-Partida E, Levresse G (2003) Fluid inclusion evolution at the La Verde porphyry copper deposit, Michocan, Mexico. J Geochem Explor 78–79:623–626

Hedenquist JW, Arribas AJ, Reynolds TJ (1998) Evolution of an intrusion-centered hydrothermal system: Far Southeast-Lepanto porphyry and epithermal Cu–Au deposits, Philippines. Econ Geol 93:373–404

Hezarkhani A, William-Jones AE (1998) Controls of alteration and mineralization in the Sungun porphyry copper deposit, Iran: evidence from fluid inclusions and stable isotopes. Econ Geol 93:651–670

Kranz RL (1983) Micro-cracks in rocks: a review. Tectonophysics 100: 449–480

Landtwing MR, Furrer C, Redmond PB, Pettke T, Guillong M, Heinrich CA (2010) The Bingham Canyon porphyry Cu–Mo–Au deposit: III. Zoned copper-gold ore deposition by magmatic vapor expansion. Econ Geol 105:91–118

Lowenstern JB (2001) Carbon dioxide in magmas and implications for hydrothermal systems. Miner Depos 36:490–502

Matsuhisa Y, Goldsmith JR, Clayton RN (1979) Oxygen isotope fractionation in the system quartz–albite–anorthite–water. Geochim Cosmochim 43:1131–1140

Mavrogenes JA, Bodnar RJ (1994) Hydrogen movement into and out of fluid inclusions in quartz: experimental evidence and geological implications. Geochim Cosmochim 58:141–148

Nabavy H (1976) An introduction to the geology of Iran. Geological survey organization of Iran, Tehran

Ohmoto H, Rye RO (1979) Isotopes of sulfur and carbon. In: Barnes HL (ed) Geochemistry of hydrothermal ore deposits, 2nd edn. Wiley, New York, pp 509–567

Pirajno F (2009) Hydrothermal processes and mineral systems. Springer, Geological Survey of Western Australia.

Prokofiev VY, Garofalo PS, Bortnikov NS, Kovalenker VA, Zorina LD, Grichuk DV, Selektor SL (2010) Fluid inclusion constraints on the

genesis of gold in the Darasun District (eastern Transbaikalia), Russia. Econ Geol 105:395–416

Roedder E (1978) Silicate liquid immiscibility in magmas and in the system of K_2O–FeO–Al_2O_3–SiO_2, an example of serendipity. Geochim Cosmochim 42:1597–1617

Roedder E (1984) Fluid inclusions. Mineral Soc America, Review in Mineralogy, 12.

Roedder E, Bodnar RJ (1980) Geologic pressure determinations from fluid inclusion studies. Annu Rev Earth Planet Sci 8:261–301

Rusk BG, Reed MH, Dilles JH, Klemm LM, Heinrich CA (2004) Compositions of magmatic hydrothermal fluids determined by LA-ICP-MS of fluid inclusions from the porphyry copper–molybdenum deposit at Butte, MT. Chem Geol 210:173–199

Rusk BG, Reed MH, Dilles JH (2008) Fluid inclusion evidence for magmatic–hydrothermal fluid evolution in the porphyry copper–molybdenum deposit at Butte, Montana. Econ Geol 103:307–333

Seedorff E, Einaudi M (2004) Henderson porphyry molybdenum system, Colorado: II. Decoupling of introduction and deposition of metals during geochemical evolution of hydrothermal fluids. Econ Geol 99: 39–72

Seedorff E, Dilles JH, Proffett JM, Einaudi MT, Zurcher L, Stavast WJA, Johnson DA, Barton MD (2005) Porphyry deposits: characteristics and origin of hypogene features. Econ Geol 100:251–298

Shahabpour J (1982) Aspects of alteration and mineralization at the Sar-Cheshmeh copper-molybdenum deposit, Kerman, Iran. Dissertation, University of Leeds.

Sharp ZD, Atudorei V, Durakiewicz T (2001) A rapid method for determination of hydrogen and oxygen isotope ratios from water and hydrous minerals. Chem Geol 178:197–210

Shepherd TJ, Rankin AH, Alderton DHM (1985) A practical guide to fluid inclusion studies. Blackie, Glasgow

Shinohara H and Kazahaya K (1995) Degassing processes related to magma chamber crystallization. In: Thompson JFH (ed) Magmas, Fluids and Ore Deposits. Mineral Assoc Canada, Short Course Series 23:47–70.

Sillitoe RH (2000) Gold-rich porphyry deposits: descriptive and genetic models and their role in exploration and discovery. SEG Rev 13: 315–345

Simmonds V (2010) Studies of geology, geochemistry and genesis of porphyry-type copper mineralization in Kighal and Barmolk areas, north of Varzeghan, East-Azarbaidjan, Iran. Dissertation, University of Tabriz.

Simmonds V (2013) Geochemistry and petrogenesis of an adakitic quartz-monzonitic porphyry stock and related cross-cutting dike suites, Kighal, northwest Iran. Int Geol Rev 55:1126–1144

Simmonds V, Calagari AA, Moayyed M, Jahangiri A (2010) Petrologic and petrogenetic study of Kighal porphyry stock (north of Varzeghan, East-Azarbaidjan province, NW Iran). Iran J Geol 13:47–60

Simmonds V, Calagari AA, Moayyed M, Jahangiri A (2012) The study of porphyry-type alteration zones and geochemical behavior of the trace and rare earth elements within them in Kighal, north of Varzeghan, East-Azarbaidjan, Iran. Iran J Crystallogr Miner 19:565–578

Sterner SM, Hall DL, Bodnar RJ (1988) Synthetic fluid inclusions: V. Solubility relations in the system NaCl–KCl–H_2O under vapor-saturated conditions. Geochim Cosmochim 52:989–1005

Taylor HP Jr (1979) Oxygen and hydrogen isotope relationships in hydrothermal mineral deposits. In: Barnes HL (ed) Geochemistry of hydrothermal ore deposits, 2nd edn. Wiley, New York, pp 236–277

Taylor BE (1992) Degassing of H_2O from rhyolite magma during eruption and shallow intrusion, and the isotopic composition of magmatic water in hydrothermal system. Geol Surv Jpn Rep 279:190–195

Ulrich T, Guenther D, Heinrich CA (2001) The evolution of a porphyry Cu–Au deposit, based on LA-ICP-MS analysis of fluid inclusions: Bajo de la Alumbrera, Argentina. Econ Geol 96:1743–1774

Vollbrecht A (1989) Microriβ-Analyse im KTB-Datenerhebung U-Tisch Mikroskopie. Unpublished report IGDL, Gottingen

Wanhainen C, Broman C, Martinsson O (2003) The Aitik Cu–Au–Ag deposit in northern Sweden: a product of high salinity fluids. Miner Depos 38:715–726

Wilkinson JJ (2001) Fluid inclusions in hydrothermal ore deposits. Lithos 55:229–272

Wilson JWJ, Kesler SE, Cloke PL, Kelly WC (1980) Fluid inclusion geochemistry of the Granisle and Bell porphyry copper deposits, British Columbia. Econ Geol 75:45–61

Zarnab Ekteshaf Consultant Engineers (2007) Geologic and alteration studies at Kighal and Barmolk areas in 1:5000 scale. Iranian national copper industries company, Tehran

Zhang YG, Frantz JD (1987) Determination of the homogenization temperatures and densities of supercritical fluids in the system NaCl–KCl–$CaCl_2$–H_2O using synthetic fluid inclusions. Chem Geol 64:335–350

Zhang D, Xu G, Zhang W, Golding SD (2007) High salinity fluid inclusions in the Yinshan polymetallic deposit from the Le–De metallogenic belt in Jiangxi Province, China: their origin and implications for ore genesis. Ore Geol Rev 31:247–260